




RESEARCH ARTICLE

Efficient reduced-order modelling based on HODMD to predict intraventricular flow dynamics

Eneko Lazpita¹ , Jesús Garicano-Mena^{1,2}  and Soledad Le Clainche^{1,2} 

¹ETSI Aeronáutica y del Espacio – Universidad Politécnica de Madrid, Madrid, Spain

²Center for Computational Simulation (CCS), Boadilla del Monte, Spain

Corresponding author: Eneko Lazpita; Email: e.lazpita@upm.es

Received: 30 July 2025; **Revised:** 4 November 2025; **Accepted:** 1 December 2025

Keywords: cardiac flow; computational fluid dynamics; left ventricle model; machine learning; reduced order model

Abstract

Accurate and efficient modelling of cardiac blood flow is crucial for advancing data-driven tools in cardiovascular research and clinical applications. Recently, the accuracy and availability of computational fluid dynamics methodologies for simulating intraventricular flow have increased. However, these methods remain complex and computationally costly. This study presents a reduced-order model (ROM) based on higher-order dynamic mode decomposition (HODMD). The proposed approach enables accurate reconstruction and long-term prediction of left ventricle flow fields. The method is tested on two idealized ventricular geometries exhibiting distinct flow regimes to assess its robustness under different hemodynamic conditions. By leveraging a small number of training snapshots and focusing on the dominant periodic components representing the physics of the system, the HODMD-based model accurately reconstructs the flow field over entire cardiac cycles and provides reliable long-term predictions beyond the training window. The reconstruction and prediction errors remain below 5 % for the first geometry and below 10 % for the second, even when using as few as the first three cycles of simulated data, representing the transitory regime. Additionally, the approach reduces computational costs with a speed-up factor of at least 10^5 compared with full-order simulations, enabling fast surrogate modelling of complex cardiac flows. These results highlight the potential of spectrally constrained HODMD as a robust and interpretable ROM for simulating intraventricular hemodynamics. This approach shows promise for integration in real-time analysis and patient specific models.

Impact statement

Understanding how blood flows inside the human heart is critical for improving cardiovascular diagnostics and treatments. This study explores how swirling blood flow patterns, known as vortex rings, form and evolve within the left ventricle, the chamber responsible for pumping oxygenated blood throughout the body. By using a combination of high-fidelity computer simulations and advanced data analysis tools, we identify the key flow structures that emerge during the filling phase of the heartbeat and how these are affected by heart geometry. Our approach also produces a highly efficient reduced-order model that can predict the future evolution of blood flow from only a short initial input. This has the potential to enable real-time simulations of cardiac function, which could assist clinicians in diagnosing heart dysfunction, designing patient-specific treatment plans or optimizing prosthetic heart devices. More broadly, this work bridges fundamental fluid mechanics with translational tools for healthcare and biomedical engineering.

1. Introduction

Cardiovascular diseases remain the leading cause of mortality worldwide, with heart failure representing a major source of morbidity and a significant reduction in quality of life (World Health Organization 2024). In this context, understanding and predicting intraventricular blood flow dynamics is essential to improving diagnosis, prognosis, and treatment planning in patients with cardiac dysfunction (see Kilner *et al.* 2000; Thomas & Popovic 2006). The left ventricle (LV), as the main pumping chamber of the heart, plays a central role in cardiac output, and its hemodynamics are intimately linked to both structural integrity and functional performance (Pedrizzetti & Domenichini 2015; Sengupta *et al.* 2006).

Computational fluid dynamics (CFD) has emerged as a powerful tool for investigating intraventricular flows, complementing *in vivo* measurements by enabling detailed, controllable exploration of flow patterns. Numerous studies have applied CFD to both idealized and patient-specific LV geometries, providing valuable insights into vortex dynamics, energy dissipation and wall shear stresses. For instance, Spandan *et al.* (2017) introduced a parallel interaction potential approach coupled with the immersed boundary method for fully resolved fluid–structure interaction simulations of deformable cardiac structures. This methodology has been extended to simulate healthy and pathological ventricles with natural and prosthetic mitral valves (Meschini *et al.* 2018), as well as to investigate systolic anterior motion in hypertrophic cardiomyopathy (Meschini, Mittal & Verzicco 2021).

Domenichini *et al.* (2005) conducted early numerical studies on the three-dimensional inflow into a ventricular-shaped cavity. They later complemented this with experimental validation (Domenichini *et al.* 2007), providing deeper insights into the mechanisms driving intraventricular flow. More recently, they explored the interaction between myocardial motion and fluid dynamics, demonstrating how alterations in tissue displacement are reflected in hemodynamic force distributions (Domenichini & Pedrizzetti 2016). Quarteroni *et al.* (2017) have developed advanced frameworks for cardiac modelling that combine electromechanics, fluid dynamics and patient-specific data (Africa *et al.* 2024; Quarteroni *et al.* 2017). These contributions reinforce the value of CFD as a predictive tool in cardiac research.

These works represent only a small sample of the growing body of literature. A comprehensive overview of CFD-based cardiac flow simulations, including their application to vortex ring (VR) analysis, is provided in the review by Nagargoje *et al.* (2025). The VR forms during early diastolic filling and plays a critical role in the efficient reorientation of the blood influx towards the aortic valve throughout the cardiac cycle. Its formation and stability are closely tied to ventricular geometry, wall motion and pathological changes, making it a relevant biomarker for cardiovascular health. In a recent study (see Lazpita *et al.* 2025), we analysed the physical mechanisms underlying VR dynamics in two idealized LV geometries, identifying the VR as the dominant flow structure driving the system's temporal evolution and highlighting its potential as a diagnostic indicator.

Despite these advancements, generating high-fidelity CFD simulations of cardiac flows remains computationally demanding. The need to account for large deformations, moving boundaries and physiologically realistic conditions results in considerable computational cost. Moreover, many CFD solvers suffer from numerical instability when applied to complex ventricular geometries or pathological flow regimes, often requiring extensive tuning or simplification of the physical model. These challenges restrict the scope of CFD applications in both clinical and research contexts.

As a result, many studies are constrained to a limited number of cardiac cycles, often fewer than five, impeding the statistical robustness and generalizability of the resulting data (Kheradvar *et al.* 2012; Chnafa *et al.* 2014). This limitation poses a significant barrier to the development of data-driven models, which require temporally rich datasets to achieve reliable performance across varying cardiac conditions.

In order to address these challenges, a novel reduced-order model (ROM) is proposed. This model is designed to accelerate the obtention of intraventricular flow databases as an alternative to high-fidelity CFD simulations. Although ROMs are widely used in fluid mechanics to reduce computational cost, their application to cardiac hemodynamics is still limited. This is mainly due to the complexity of the problem, which involves large deformations, moving boundaries, strong nonlinearities and fluid–structure interaction (Ballarin *et al.* 2016; Lassila *et al.* 2014). Our method extends the capabilities of existing modal decomposition frameworks by leveraging the higher-order dynamic mode decomposition

(HODMD) algorithm (Le Clainche & Vega 2017a). The HODMD technique extracts the dominant coherent structures of the flow and models their temporal evolution. In doing so, it captures the underlying physics, most notably the VR dynamics that govern early diastolic filling in the LV.

Although HODMD has been successfully applied in simplified fluid scenarios, such as bluff body wakes or laminar shear flows (Le Clainche & Vega 2017b), this work presents its first application, to the authors' knowledge, to cardiac flows. In this context, we address additional challenges inherent to cardiac flow simulations, such as significant domain deformation driven by myocardial motion (i.e. involving moving meshes). These complexities are further augmented by the influence of the ventricular wall on VR dynamics, as well as by the substantial temporal variability in velocity and pressure fields throughout the cardiac cycle, driven by the strong coupling between geometry deformation and flow evolution. By adapting the ROM to the spatiotemporal characteristics of the data, we achieve significant computational savings while preserving the essential dynamics of the system.

Recent advances in deep learning have introduced a variety of architectures, such as autoencoders, convolutional neural networks and recurrent models, for data-driven flow reconstruction and ROM (Sanchis-Agudo *et al.* 2024; Solera-Rico *et al.* 2024). These approaches can offer rapid predictions once trained, but they typically require a problem-specific network design and extensive hyperparameter tuning to ensure both numerical stability and physical consistency. In contrast, the HODMD framework employed in this study extracts dominant coherent structures and their characteristic frequencies directly from data, without the need for prior assumptions about the underlying dynamics or geometry. This provides a more interpretable, physics-grounded representation of the flow while maintaining competitive accuracy with significantly lower model complexity.

The following sections are structured as follows: § 2 introduces the ROM methodology based on HODMD and its implementation. Section 3 presents the two idealized LV databases used in this study. In § 4, we provide a detailed analysis of the ROM configuration using two distinct idealized LV geometries. Finally, § 5 summarizes the main findings and discusses future directions.

2. Reduced-order modelling

As mentioned, the ROM employed in this study is based on HODMD, a data-driven technique that extracts dominant spatiotemporal patterns from complex dynamical systems. To handle the inherently high-dimensional nature of the simulation data, we adopt a tensor-based extension of the algorithm, known as multidimensional HODMD (mdHODMD) (Hetherington *et al.* 2024). This formulation allows us to preserve the multidimensional structure of the dataset and enhance both computational efficiency and interpretability.

The input data consists of time-resolved three-dimensional velocity fields obtained from CFD simulations. For each time instant, the velocity field is represented by three components defined over a structured grid in three spatial directions. By stacking all temporal snapshots together, the dataset can be naturally arranged as a five-dimensional tensor $V \in \mathbb{R}^{J_1 \times J_2 \times J_3 \times J_4 \times K}$, where

- (i) $J_1 = 3$ corresponds to the velocity components (v_x, v_y, v_z) ,
- (ii) J_2, J_3, J_4 represent the spatial discretization density along the three coordinate directions and
- (iii) K denotes the number of time steps.

The mdHODMD algorithm is then applied to this tensor in three consecutive main steps: dimensionality reduction via tensor decomposition, extraction of dynamic modes and their associated frequencies, and prediction of the system's temporal evolution.

2.1. Data dimensionality reduction

The processing of large-scale datasets directly poses a significant computational challenge, requiring the implementation of dimensionality reduction techniques to ensure manageability. Singular value

decomposition (SVD) (Sirovich 1987) is widely used in fluid dynamics to reduce data dimensionality and filter out noise. However, the intraventricular flow simulations considered in this work are high-dimensional, transient and highly nonlinear. They involve moving geometries subject to large temporal deformations and complex spatiotemporal patterns that appear. As a result, more advanced techniques are required to analyse and predict their behaviour effectively. In this study, we apply the high-order singular value decomposition (HOSVD) (Le Clainche & Vega 2017a), a tensor-based extension of SVD that enables simultaneous decomposition along multiple data dimensions. This method improves compression and noise filtering by decoupling the modes in each dimension. As a result, it can distinguish and eliminate noise or redundancies independently across spatial, temporal and physical-magnitude components. Such enhanced denoising and compression capabilities make HOSVD particularly well-suited for building robust, low-rank representations from transient flow data (Groun *et al.* 2025), thereby supporting the construction of accurate and efficient predictive models.

The HOSVD is applied to the fifth-dimensional tensor \mathbf{V} , which in turn is factorized as

$$\mathbf{V}_{j_1 j_2 j_3 j_4 k} \approx \sum_{p_1=1}^{P_1} \sum_{p_2=1}^{P_2} \sum_{p_3=1}^{P_3} \sum_{p_4=1}^{P_4} \sum_{n=1}^N \mathbf{S}_{p_1 p_2 p_3 p_4 n} \mathbf{W}_{j_1 p_1}^{(v)} \mathbf{W}_{j_2 p_2}^{(x)} \mathbf{W}_{j_3 p_3}^{(y)} \mathbf{W}_{j_4 p_4}^{(z)} \mathbf{T}_{kn}, \quad (2.1)$$

where $\mathbf{S}_{p_1 p_2 p_3 p_4 n}$ is the fifth-dimensional core tensor, and the orthonormal matrices $\mathbf{W}^{(v)}$, $\mathbf{W}^{(x)}$, $\mathbf{W}^{(y)}$, $\mathbf{W}^{(z)}$ and \mathbf{T} contain the SVD modes for each dimension. A tuneable tolerance ε determines the number of retained modes N , ensuring that $\sigma_{N+1}^{(j)} / \sigma_1^{(j)} \leq \varepsilon_1$ with $j = 1, \dots, 5$. This temporal matrix \mathbf{T} containing the temporal coefficients associated with each mode (of dimensions $N \times K$) serves as input for the subsequent dynamic mode decomposition (DMD) computation.

2.2. Calculation of DMD modes

Dynamic mode decomposition (Schmid 2010) provides a ROM approach by expressing complex spatiotemporal data as a linear combination of M coherent structures, or modes, that evolve in time. The approximation of the dataset $\mathbf{V}_{j_1}(x, y, z, t_k)$ (where $j_1 = 1, \dots, 3$ indexes the velocity components) is formulated as

$$\mathbf{V}_{j_1}(x, y, z, t_k) \approx \sum_{m=1}^M a_m \mathbf{u}_m(x, y, z) e^{(\delta_m + i\omega_m)t_k} \quad \text{for } k = 1, \dots, K, \quad (2.2)$$

where \mathbf{u}_m denotes the spatial structure of each DMD mode, a_m is the mode amplitude, δ_m is the temporal growth rate and ω_m represents the oscillation frequency.

To obtain these modes, DMD assumes a linear mapping between consecutive data snapshots $\{\mathbf{v}_1, \mathbf{v}_2, \dots, \mathbf{v}_K\}$, posing the relation to be described as

$$\mathbf{V}_2^K \approx \mathbf{R} \mathbf{V}_1^{K-1}, \quad (2.3)$$

where \mathbf{R} is a linear operator that approximates the underlying dynamics, effectively capturing the temporal progression through the so-called Koopman framework (Mezić 2013; Otto & Rowley 2021).

Higher-order DMD (Le Clainche & Vega 2017a) extends standard DMD by incorporating multiple time-delayed snapshots, enhancing robustness and accuracy in capturing complex flow structures. Furthermore, the mdHODMD algorithm preserves the tensorial formulation by applying the higher-order Koopman assumption to the temporal matrix \mathbf{T} extracted in the previous step using HOSVD (see (2.1)) as

$$\mathbf{T}_{d+1}^K \approx \widehat{\mathbf{R}}_1 \mathbf{T}_1^{K-d} + \widehat{\mathbf{R}}_2 \mathbf{T}_2^{K-d+1} + \dots + \widehat{\mathbf{R}}_d \mathbf{T}_d^{K-1}. \quad (2.4)$$

This formulation links each snapshot to d previous time steps, capturing intricate temporal dynamics beyond what standard DMD offers. The modified Koopman matrix $\widehat{\mathbf{R}}$, which contains all the linear operators $(\widehat{R}_1, \widehat{R}_2, \dots, \widehat{R}_d)$, is then computed to extract the DMD modes. Another tuneable tolerance is introduced for the HODMD; in this work, and following the guidelines discussed in Le Clainche & Vega

(2017a) and Hetherington *et al.* (2024) which is set equal to the one selected for the HOSVD, such that $\varepsilon_1 = \varepsilon_2 = \varepsilon$.

2.3. Prediction

Once the data is decomposed into DMD modes, future-state predictions are obtained by evaluating (2.2) at time instants beyond the training window $t > t_K$. Specifically, the model is constructed using data within the interval $t \in [0, pT]$, where T is the period of the cardiac cycle and p is the number of cycles employed for training. In this work, we will consider $p \in \mathbb{R}$ and $p \leq 10$. The resulting ROM is then used to predict the flow dynamics in a later interval, namely $t \in [10T, 20T]$, allowing us to assess the long-term predictive capabilities of the method.

The way modes are selected plays a crucial role in ensuring prediction accuracy and stability in the model. Depending on the calibration of the algorithm, spurious modes unrelated to the underlying physics may be captured, typically associated with noise or numerical artefacts. As a result, using all computed M DMD modes can degrade the quality of the extrapolated prediction. To address this difficulty, we adopt a filtering strategy in which only those modes with growth rates lower than a certain threshold are deemed physically relevant and retained for prediction. This threshold is set with a tuneable growth rate value δ_{tune} . Thus, stable modes will correspond to $-\delta_{tune} < \delta_m < 0$ with $\delta_{tune} > 0$. Almost all of the selected modes correspond to frequencies associated with the dominant dynamics of the system.

Furthermore, when working with transient simulation data, certain modes, although physically relevant, may exhibit highly negative growth rates, leading to their rapid attenuation over time. This offers the potential to enhance the temporal stability of the model predictions; we also construct an alternative formulation in which we enforce $\delta_m = 0$, thereby eliminating exponential decay. This modification prevents excessive damping of key flow structures and enables more reliable long-term forecasts of the intraventricular dynamics.

To assess the accuracy of the ROM, we analyse the absolute error distribution over the entire dataset by computing the histogram of the normalized absolute error, defined as

$$E(\%) = \frac{|\mathbf{v} - \mathbf{v}_{\text{pred}}|}{\max |\mathbf{v} - \mathbf{v}_{\text{pred}}|} \times 100, \quad (2.5)$$

where \mathbf{v} denotes the reference simulation data and \mathbf{v}_{pred} is the reconstructed prediction. The normalization factor corresponds to the maximum absolute error computed independently for each velocity component, considering all spatial locations and time steps in the domain.

The number of bins in the histogram is determined using Sturges's formula, applied to the spatial grid,

$$N_{\text{bins}} = 1 + \log_2(N_{\text{grid}}), \quad (2.6)$$

where $N_{\text{grid}} = N_x \times N_y \times N_z$ represents the total number of spatial points. In our case, this results in approximately 20 bins, allowing for an intuitive interpretation: the first bin represents the relative frequency of errors within the range 0%–5%, the second within 5%–10%, and so forth.

A key advantage of the ROM is its drastic reduction in computational cost. In this study, this increase in computational efficiency is quantified using the speed-up factor (SUF), defined as

$$\text{SUF} = \frac{t_{\text{CFD}} \times N_{\text{CPU}}}{t_{\text{ROM}}} \quad (2.7)$$

where t_{CFD} is the runtime of the full-order CFD simulation, N_{CPU} is the number of processors used, and t_{ROM} is the time required for the ROM prediction.

Finally, we note that the HODMD-based ROM involves several tuneable parameters that require careful calibration. These include the truncation tolerance ε , which controls the number of modes retained; the window size d , which determines the number of snapshots used in each HODMD window; and the threshold δ_{tune} applied to the growth rates to distinguish physically relevant modes from spurious

Table 1. Non-dimensional geometric parameters for the two idealized ventricular models, using base radius a as reference length.

Parameter	Ideal 1 (Zheng <i>et al.</i> 2012)	Ideal 2 (Vedula <i>et al.</i> 2014; Kjeldsberg <i>et al.</i> 2023)
Chamber length ratio b/a	4.0	2.2
Inlet diameter D/a	1.2	0.85
Outlet diameter d/a	0.4	0.6
Tube height H/a	2.4	2.7
Inlet offset C/a	0.275	0.35
Outlet offset c/a	0.675	0.6
Reference radius a [cm]	2.0	2.9

ones. To calibrate the ROM, multiple combinations of ε and d are explored during training. While ε is adjusted depending on the noise level, d is typically chosen between 15%–50% of the total snapshots. Once the physical modes are identified, their growth rates and frequencies are analysed to set an appropriate threshold δ_{tune} , ensuring that only persistent, physically meaningful modes are retained for prediction. This procedure enhances the robustness and accuracy of the resulting ROM.

To calibrate the HODMD-based ROM, multiple combinations of the truncation tolerance ε and the window size d are explored. The tolerance ε is adjusted depending on the noise present in the data, whereas d is typically chosen to be between 10%–50% of the total snapshots (Le Clainche *et al.* 2020; Hetherington *et al.* 2024). After identifying the physical modes, their growth rates and frequencies are analysed to define a threshold that separates persistent modes from spurious ones, ensuring the robustness of the ROM construction.

3. Flow dynamics

To evaluate the performance of the ROM introduced earlier, we apply it to two distinct datasets, both representing idealized LV geometries. The first model, referred to as `Ideal 1`, consists of a semiellipsoidal chamber extracted from Zheng *et al.* (2012) and will be used to develop and illustrate the methodology. The second model, `Ideal 2`, has a smoother, more rounded chamber shape and has been studied in prior works (Vedula *et al.* 2014; Kjeldsberg, Sundnes & Valen-Sendstad 2023). This model will serve as an additional test case to evaluate the robustness of the approach under different conditions.

3.1. Database

To ensure that the idealized geometries represent physiologically realistic left ventricular conditions, particularly the end-systolic volume that corresponds to the minimum volume at the end of systole, we define a set of non-dimensional geometric parameters. These parameters are expressed in table 1 using the base radius a of the ventricular chamber as the reference length for each model.

A schematic representation of these parameters and their spatial arrangement is provided in figure 1, illustrating the geometry and orientation of each feature. The figure also identifies the symmetry plane A–A' (located at $y = 0$) used throughout the analysis (highlighted in blue). Additionally, a probe line (L1), indicated in red, is defined to extract temporal data at specific spatial locations. For the `Ideal 1` model, L1 is located at $x/a = 0$, $y/a = 0$, and it extends through all the vertical z of the chamber. For the `Ideal 2` model, L1 is positioned at $x/a = 0$, $y/a = 0$, and again it takes all the chamber height.

Using the two idealized geometries of the LV, we conducted CFD simulations to investigate intraventricular flow dynamics. Simulations were carried out using the solver Ansys Fluent (Ansys, Inc. 2023). In both cases, blood was modelled as an incompressible Newtonian fluid with constant density $\rho = 1060 \text{ kg m}^{-3}$ and dynamic viscosity $\mu = 0.004 \text{ Pa s}$.

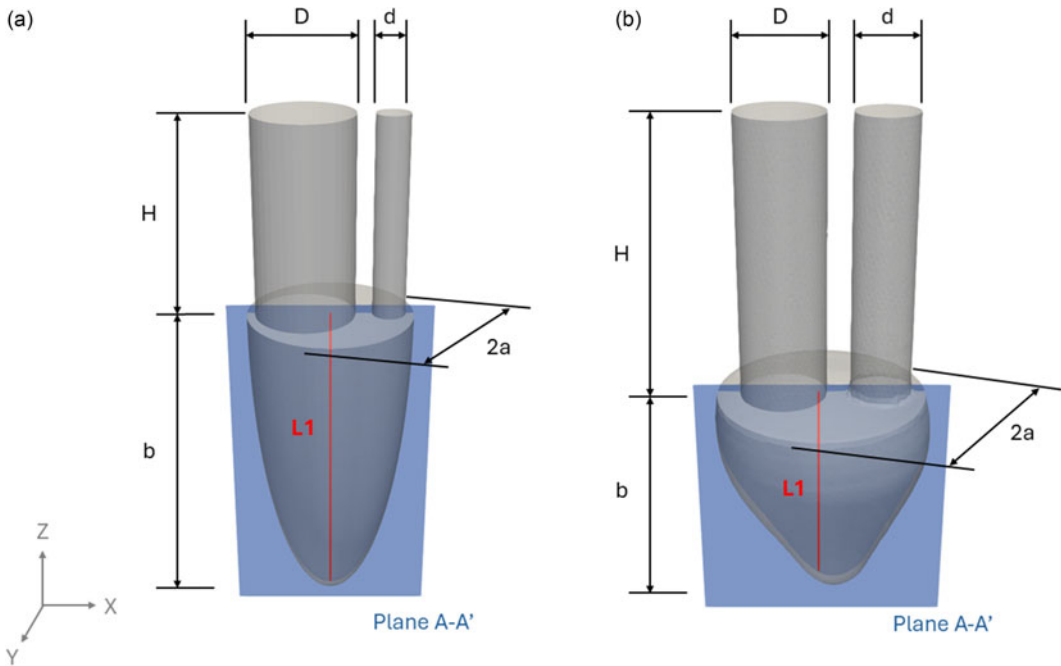


Figure 1. Representation of both idealized LV models: (a) *Ideal 1* and (b) *Ideal 2*. Blue, symmetry plane A–A' used for two-dimensional visualization; red, probe line L1 to represent temporal data.

To characterize the flow regime, we computed the Reynolds number (Re) based on the inlet tube diameter D (non-dimensionalized as D/a) and the peak inlet velocity V_{\max} over the cardiac cycle. The resulting Reynolds numbers were approximately $Re \approx 5500$ for the *Ideal 1* model and $Re \approx 4900$ for *Ideal 2*. Despite these values indicating transitional or potentially turbulent flow, we assumed a laminar regime, in line with previous studies (He *et al.* 2022; Tagliabue, Dedè & Quarteroni 2017), where coherent vortex structures, such as the main VR, were accurately captured under laminar assumptions.

A zero-velocity initial condition is set in the simulation pipeline for both models. Moreover, for both simulations, pressure-based boundary conditions were set at the inlet and outlet. These boundaries dynamically alternated between open and closed states to represent the cardiac cycle: during diastole, the inlet was open and the outlet treated as a wall; during systole, the roles were reversed. This boundary-switching was complemented by the dynamic motion of the ventricular wall, imposed by prescribing an interpolated sequence of meshes corresponding to each time instant. This approach induces pressure gradients within the chamber that drive blood in and out, thereby mimicking physiological behaviour.

The simulation framework and its assumptions were extensively validated in previous studies (Lazpita *et al.* 2024a,b, 2025), including convergence analyses and comparisons with benchmark data. All numerical simulations were performed on the high-performance computing cluster Magerit, hosted at CeSViMa (Centro de Supercomputación y Visualización de Madrid). The computations were parallelized using 40 message passing interface (MPI) tasks within a single node.

For the rest of the manuscript, time is non-dimensionalized using the period T , such that $t^* = t/T$. This normalization allows for a consistent comparison of corresponding time instants across both simulation databases. It is also important to note that, for the first geometry, the diastolic phase takes place within the interval $t^* \in [i, i + 0.67]$, followed by the systolic phase in $t^* \in [i + 0.67, i + 1]$. In contrast, for the second geometry, diastole spans $t^* \in [i, i + 0.8]$, and systole occurs within $t^* \in [i + 0.8, i + 1]$, where i denotes the cycle index.

A key aspect of intraventricular hemodynamics is the formation and evolution of a VR during diastole, triggered by the inflow through the mitral valve (Nagargoje *et al.* 2025). This structure undergoes tilting

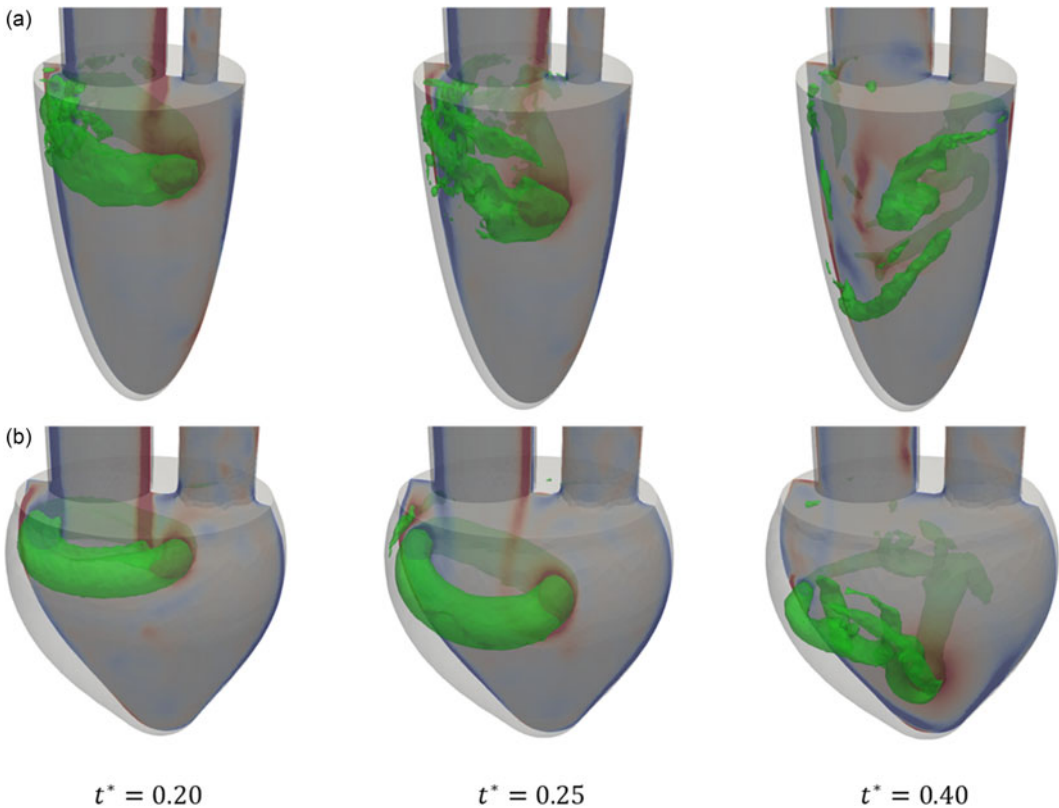


Figure 2. Representative snapshots of the intraventricular flow fields for *Ideal 1* (a) and *Ideal 2* (b). Green, Q -criterion isosurface at 2500; background, vorticity in the symmetry plane; range $[-100, 100]$.

and eventual breakdown due to instabilities, and its dynamics are considered a primary indicator of pumping efficiency. Accurately capturing the VR behaviour is, therefore, essential.

Figure 2 illustrates representative time instants for both geometries. The green isocontours show the Q -criterion at a level of 2500, highlighting vortex cores, while the colormap on the symmetry plane displays the out-of-plane vorticity in the range $[-100, 100] \text{ s}^{-1}$. Notably, the VR in *Ideal 1* dissipates earlier than in *Ideal 2*; by $t^* = 0.25$, the ring in *Ideal 1* is already breaking up, whereas *Ideal 2* still maintains a coherent and smooth structure. Even at $t^* = 0.40$, the second model, though deformed, maintains a closed VR, while the first model's ring has fully dissipated.

As shown in Lazpita *et al.* (2025), the vortex breakdown process is strongly influenced by ventricular geometry. In the *Ideal 1* configuration, which features a narrower chamber, the vortex interacts with the ventricular wall at an earlier stage. This early interaction triggers the breakdown process before the VR can reach the apex. In contrast, the *Ideal 2* model, with a wider chamber, allows the VR to fully develop, travel towards the apex, and break down as a combination of a reduction in velocity and wall interaction.

These contrasting behaviours can be attributed to two main factors:

- (i) the narrower geometry of *Ideal 1* causes the vortex to interact more strongly with the ventricular walls, preventing it from reaching the apex and accelerating its breakdown;
- (ii) *Ideal 2* exhibits a lower ejection fraction and volume change, resulting in reduced pressure gradients and slower flow dynamics.

These differences in VR dynamics will be key for assessing the ROM's ability to capture flow physics across varying conditions.

Table 2. Summary of simulation cases used to build and evaluate the ROM discussed in § 2, including the number of cardiac cycles p , normalized time intervals t^* , snapshot count K , their intended purpose and the selected tuneable growth rate parameter δ_{tune} .

Case	p	Time interval t^*	Snapshots K	Purpose	δ_{tune}
T-1.5	1.5	[0, 1.5]	30	Training (transient)	1.0
T-3	3	[0, 3]	60	Training (transient)	0.5
T-10	10	[0, 10]	200	Training (transient)	0.01
V-10	10	[10, 20]	200	Validation (converged)	0.01

Each simulation database consists of 20 cardiac cycles, with flow fields sampled at a time interval of $\Delta t^* = 0.05$: therefore, these are 20 snapshots per cycle and a total of $K = 400$ snapshots. For training the ROM, we use data from the first 10 cycles, which include the initial transient phase. The remaining 10 cycles are reserved for validation, as they capture the dynamics once the system has reached temporal convergence. This distinction is further supported by the application of DMD, which reveals that growth rates stabilize only in the latter cycles.

Although it is common practice in the literature to simulate up to six cycles, we shall find that the flow remains in a transient state at that point (Canè *et al.* 2022; Grünwald *et al.* 2022; Korte *et al.* 2023). This highlights the importance of longer simulations to ensure the reliability of the ROM and the physical relevance of the extracted modes.

The cases listed in table 2 are analogous for both LV geometries and thus we maintain the same denomination for consistency and brevity. Each case corresponds to a specific time window and number of cycles, which are used either for training or validation of the ROM. We also report the tuneable growth rate value selected for each case, which enables the identification of persistent modes that represent the main dynamics of the system, effectively discarding the spurious modes extracted by HODMD.

3.2. Database sensitivity assessment

Despite careful simulation set-up, the complex nature of moving-wall CFD simulations introduces inherent variability across cycles, even setting the boundary conditions perfectly periodic (Chnafa *et al.* 2014). While major flow structures, such as the primary VR, secondary vortices and outflow jets, are consistently reproduced, smaller-scale features might vary.

We quantify the variability across cardiac cycles by analysing the cycle-to-cycle variation of the total kinetic energy (TKE), defined at each non-dimensional time instant t^* as

$$\text{TKE}(t^*) = \int_{V(t^*)} \frac{1}{2} \rho \mathbf{v}^2 dV, \quad (3.1)$$

where $V(t^*)$ is the time-dependent ventricular volume, ρ is the fluid density, and \mathbf{v} is the velocity vector. The TKE integrated over each cardiac cycle is computed as

$$\text{TKE}_i = \int_{i-1}^i \text{TKE}(t^*) dt^*, \quad i = 1, \dots, 20, \quad (3.2)$$

where i , again, denotes the index of the cycle. To measure convergence and variability, we evaluate the relative root mean square error (RRMSE) of each cycle with respect to the last one,

$$\text{RRMSE}_{\text{TKE}}(\%) = \frac{|\text{TKE}_{20} - \text{TKE}_i|}{|\text{TKE}_{20}|} \times 100, \quad (3.3)$$

where TKE_{20} is the integrated kinetic energy for the 20th cycle, considered as the reference.

Figure 3 illustrates the cycle-to-cycle variability in TKE error, expressed as the RRMSE for both *Ideal 1* and *Ideal 2* geometries. Remember that the simulation was initialized from a zero-velocity condition. After the initial transient, the RRMSE remains below 4% across all subsequent cycles,

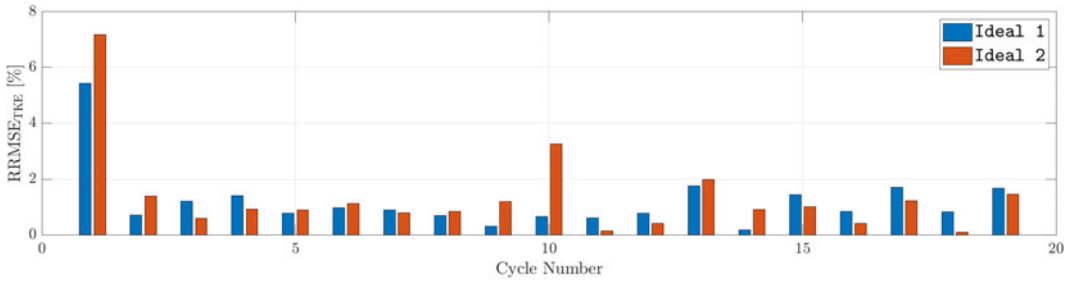


Figure 3. Cycle-to-cycle RRMSE of TKE for Ideal 1 and Ideal 2, visualized using a grouped bar plot.

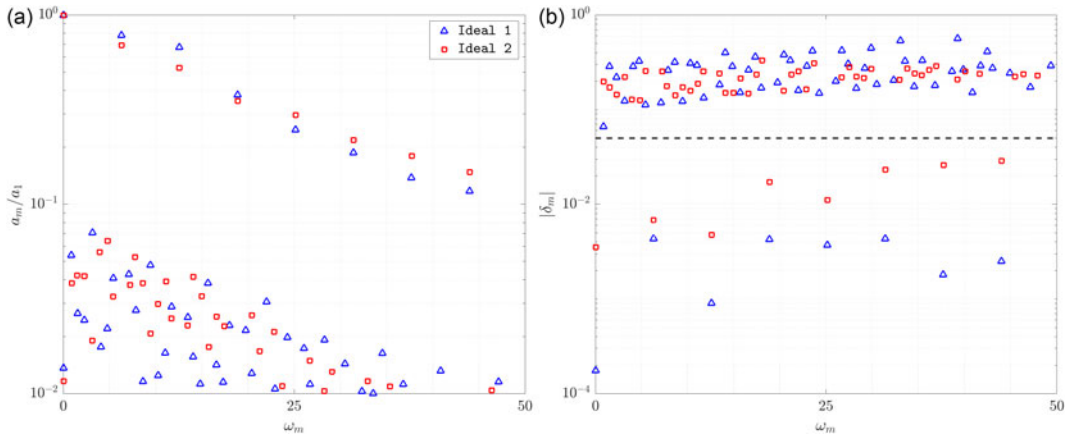


Figure 4. Spectrum of DMD modes for both idealized models: normalized amplitude versus frequency (a) and absolute value of growth rate versus frequency (b). The dashed line at $\delta_{tune} = 5 \times 10^{-2}$ in (b) separates persistent physical modes from transient or spurious ones.

indicating good reproducibility of global flow features. However, local flow characteristics, such as instantaneous velocity fields, may still exhibit larger discrepancies due to intrinsic variability in the numerical solution (Chnafa et al. 2014; Canè et al. 2022). As such, predictions obtained from ROMs should be interpreted within a baseline uncertainty margin of approximately 5%–10%.

3.3. True frequency analysis

Figure 4 presents the DMD spectra obtained from a representative HODMD calibration applied to both Ideal 1 and Ideal 2 cases. Figure 4(a) shows the normalized amplitude of each mode with respect to frequency, while figure 4(b) displays the corresponding absolute values of the growth rates. Although only one calibration is depicted here for clarity, the modes shown have been previously identified as robust through an exhaustive sensitivity analysis involving the HODMD parameters d and ε , following the methodology described in Le Clainche et al. (2020) and Hetherington et al. (2024).

The amplitude spectra in figure 4(a) reveal the dominant frequencies that appear consistently across both geometries. These include the fundamental frequency $\omega = 2\pi$ and its harmonics, such as 4π , 6π and up to approximately 14π , indicating strong periodicity and physical relevance of these modes. Lower-amplitude modes, scattered throughout the spectrum, are not persistent across calibrations and are interpreted as numerical noise or transient artefacts.

Figure 4(b) provides additional insight through the analysis of growth rates $|\delta_m|$. Robust physical modes tend to have small or nearly zero-growth rates, indicating long-term persistence throughout the

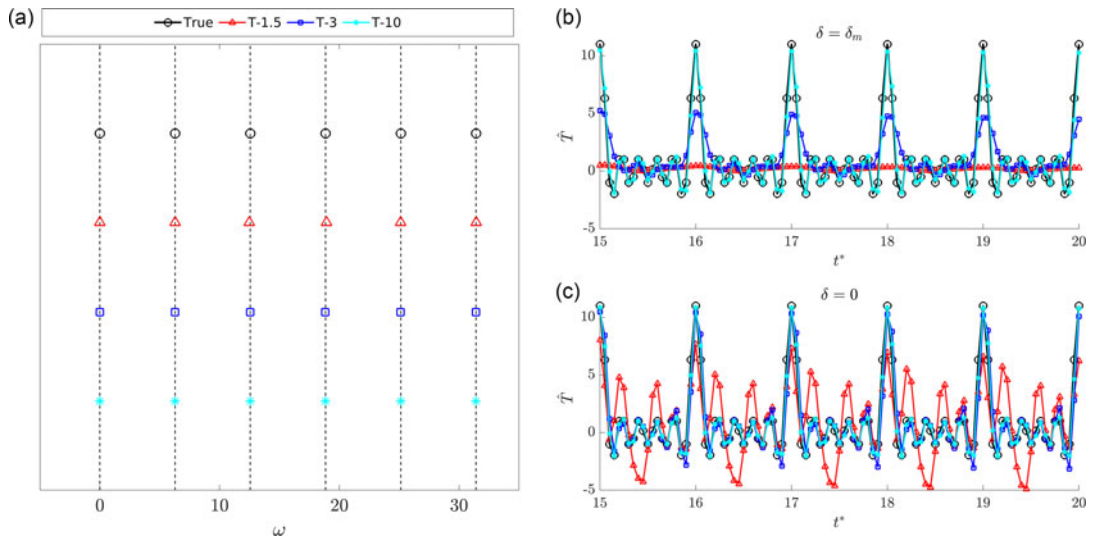


Figure 5. Comparison of (a) the calculated frequency and (b,c) temporal coefficient with HODMD with the true system (black) for the *Ideal 1* model: (b) computed growth-rate and (c) growth-rate set to zero. The cases are coloured as (red) T-1.5, (blue) T-3 and (cyan) T-10 cases (see table 2).

simulation. A threshold of $\delta_{\text{tune}} = 5 \times 10^{-2}$ (shown as a dashed line) distinguishes these physical modes from the spurious ones, which exhibit larger decay or amplification rates and lack consistency. This threshold was established based on a qualitative shift observed in the spectral structure during the calibration study: below this value, the modes were consistently identified and physically meaningful, while above it, the spectrum became irregular and inconsistent.

These results confirm that the dominant dynamics of both *Ideal 1* and *Ideal 2* models are governed by a limited number of coherent structures oscillating at fundamental and harmonic frequencies, in agreement with the known periodicity of the cardiac cycle.

While the current study focuses on filtering spurious modes to construct a robust ROM, a detailed analysis of the retained modes and their physical interpretation is presented in a complementary work (Lazpita *et al.* 2025), where the underlying flow dynamics in idealized LV models are extensively characterized. In that study, the leading modes were shown to capture the formation, tilting, and breakdown of the primary VR generated during early diastole, associated with the fundamental frequency $\omega = 2\pi$, as well as the appearance of a secondary VR during the late diastolic inflow ($\omega = 4\pi$). Higher-order modes revealed nonlinear interactions between these frequencies, describing the onset of vortex breakdown and the emergence of smaller-scale structures. This modal hierarchy thus provides a physically consistent picture of the intraventricular flow, linking coherent structures to characteristic temporal dynamics.

4. Results

4.1. Semiellipsoidal model *Ideal 1*

For the first model, HODMD is applied to analyse several training subsets, each consisting of a varying number of cardiac cycles p as defined in table 2. The objective is to determine how many cycles are necessary to accurately capture the temporal dynamics of the system. To evaluate this, we construct the temporal evolution of the system using the frequencies and growth rates extracted using HODMD. We consider two scenarios: (i) using the growth rates computed by HODMD, and (ii) setting all growth rates to zero.

Figure 5 provides a detailed evaluation of HODMD performance across different temporal window lengths. Figure 5(a) shows the estimated frequencies compared with the theoretical ones. The results

confirm that, for all cases, the dominant frequency and its harmonics are accurately captured, with minimal deviation from the true system values.

Figure 5(b,c) illustrates the reconstructed temporal coefficients \hat{T} for each case, comparing the original reconstruction that preserves the computed growth rates (figure 5b) with a modified version where all growth rates are manually set to zero (figure 5c), thereby enforcing purely periodic behaviour.

In the shortest window (T-1.5, red), the dominant frequency is already reasonably well estimated; however, the temporal coefficients show significant distortion, primarily due to an excessive negative growth rate and the inaccurate capture of higher harmonics. Suppressing growth in this case provides some improvement but remains suboptimal. For the intermediate case (T-3, blue), frequency estimates are much more precise, and enforcing zero growth yields a nearly periodic signal with minimal distortion. Finally, in the longest window (T-10, cyan), both frequency and growth rate estimates are sufficiently accurate, and the temporal evolution remains consistent with the physical oscillatory behaviour even without modifications, leaving the zero-growth correction redundant.

The results indicate that the estimated growth rate for some modes is significantly negative (e.g. $\delta \approx -0.3$), which causes an artificial attenuation of the signal over time with respect to the ground truth. Therefore, a negative growth rate leads to exponential decay, reducing the amplitude of the reconstructed signal and compromising long-term prediction accuracy. Setting the growth rate to zero significantly improves prediction stability by removing the artificial damping and better representing the periodic nature of these simulations.

Furthermore, including all modes introduces noise and spurious contributions, resulting in degraded accuracy, whereas the principal modes alone sufficiently capture the main dynamics. While 1.5 cycles are sufficient to recover the overall behaviour, at least three cycles are needed for more precise predictions.

Now that the spectral characteristics of the simulations have been shown to be accurately captured using only three cycles (when the growth rate is set to zero), we turn our attention towards the spatial support. To this end, we perform predictions using DMD modes extracted from datasets of different lengths. The analysis focuses on the most accurate configurations, which are constructed by selecting modes with a growth rate below a defined threshold and subsequently enforcing a zero-growth rate. This procedure ensures that all retained modes contribute equally over time.

Figure 6 illustrates the temporal evolution of the v_x velocity component along probe line L1. This component is particularly relevant because the flow exhibits a strong recirculating behaviour around the vortex structure within the chamber. Consequently, v_x captures the dominant dynamics. Predictions obtained from different training sets are compared with the reference case V-10. Figure 6(a) presents the predicted evolution, while figure 6(b) shows the corresponding absolute error with respect to the reference data.

The flow evolution at line L1 is influenced by both the inflow near the inlet and the recirculation induced by the VR moving towards the apex. Across all configurations, accurate predictions are obtained by selecting only the permanent, physically relevant modes. This choice effectively removes spurious contributions that would otherwise corrupt the predictions. Enforcing a zero-growth rate further improves accuracy by preventing any mode from dominating or decaying over time.

The results again show that using only 1.5 cycles of data leads to poor predictions with limited potential for improvement. Increasing the training length to three cycles significantly enhances accuracy, especially when the growth rate is set to zero, which prevents amplitude decay. Note that, even with 10 cycles, small discrepancies persist, particularly near the inlet where the inflow dominates. This reflects the intrinsic difficulty of reconstructing the complex nonlinear behaviour in that region. The overall results, despite these deviations, are consistent with the expected simulation accuracy and are considered reliable.

After evaluating the accuracy of the line evolution over time, we performed a similar analysis to evaluate quality in a larger spatial region. Figure 7 shows the two-dimensional contours of the v_z velocity component in the A–A' plane at $t^* = 19.25$ (1/4 of cycle) for the Ideal 1 case, comparing the T-1.5, T-3 and T-10 configurations (figure 7a). When compared with the reference case V-10, all configurations capture the main features of the flow field, including the inflow and recirculation zones within

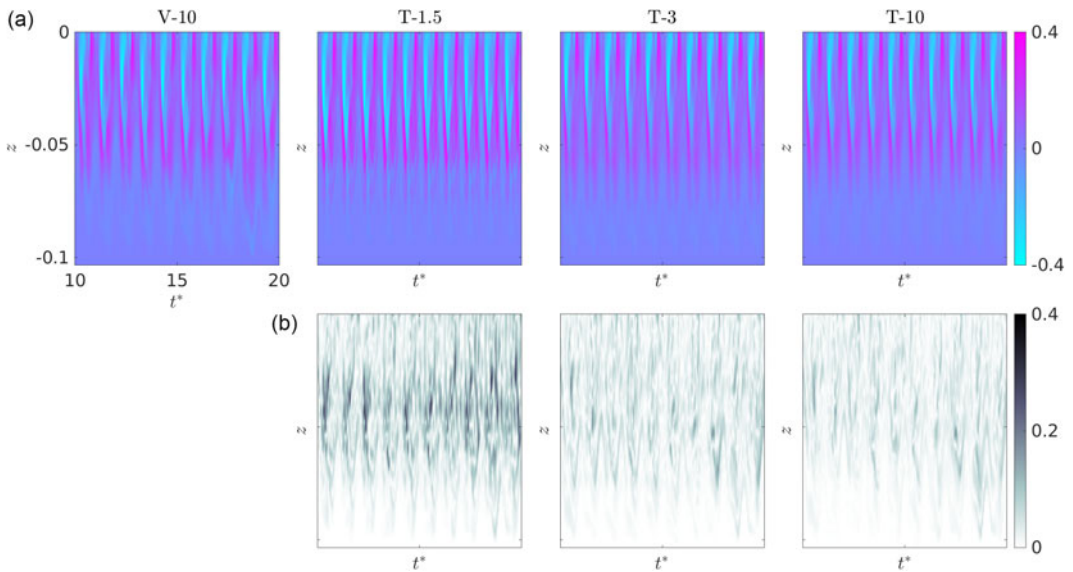


Figure 6. Temporal evolution of the v_x velocity component along centre line L1 for the *Ideal 1* case. Panel (a) shows predictions from ROMs constructed using training sets T-1.5, T-3 and T-10. Panel (b) presents the absolute error relative to the reference case V-10. All results are obtained using a subset of selected modes with an enforced zero-growth rate ($\delta = 0$).

the chamber at this time instant. However, the T-1.5 case exhibits noticeable inaccuracies, particularly a non-physical influence of the outflow that should not be present at this phase of the cycle.

The corresponding absolute error plots (figure 7b) support the previous statement, computed as the absolute difference with respect to the V-10 solution. The T-1.5 configuration shows higher overall discrepancies, especially in the outlet region. In contrast, the T-3 case significantly reduces the error, achieving accuracy levels comparable to those of the T-10 configuration, which includes many more samples.

A more quantitative evaluation of the error is shown in figure 8. Here, the error histograms for this configuration over different numbers of cycles for, again, the most accurate configurations are presented. As observed, across all cases, in at least 99% of the spatial locations, the error is below 5%, demonstrating the reliability of the ROM.

Now, instead of aggregating the error over all cycles, figure 9 presents the temporal evolution of the probability that the predicted data remain within a 5% error threshold. The results show that this probability remains above 0.7 throughout all predicted cycles, indicating consistent predictive performance. The highest accuracy is observed during systole, where the flow is mainly vertical and directed towards the outlet, exhibiting simpler dynamics. Conversely, the probability of maintaining low error decreases during diastole, reaching its minimum in the late diastolic phase, when the flow becomes fully three-dimensional, the velocity magnitudes are comparatively lower, and the range of spatial length-scales involved is larger. Additionally, the T-1.5 configuration, trained with only one and a half cycles, shows greater variability in the probability distribution, whereas larger training sets such as T-3 and T-10 yield more stable and consistent results across cycles.

It is important to acknowledge the intrinsic variability present in these types of simulations. Even when comparing different cycles of the ground truth simulation, minor discrepancies arise. Given this inherent variability, the accuracy achieved by the ROM is particularly noticeable, considering its significantly lower computational cost, which will be discussed shortly.

The greatest potential of using the ROM lies in its significant reduction of computational cost. For instance, the full-order CFD simulation was executed using 40 central processing units (CPUs) and

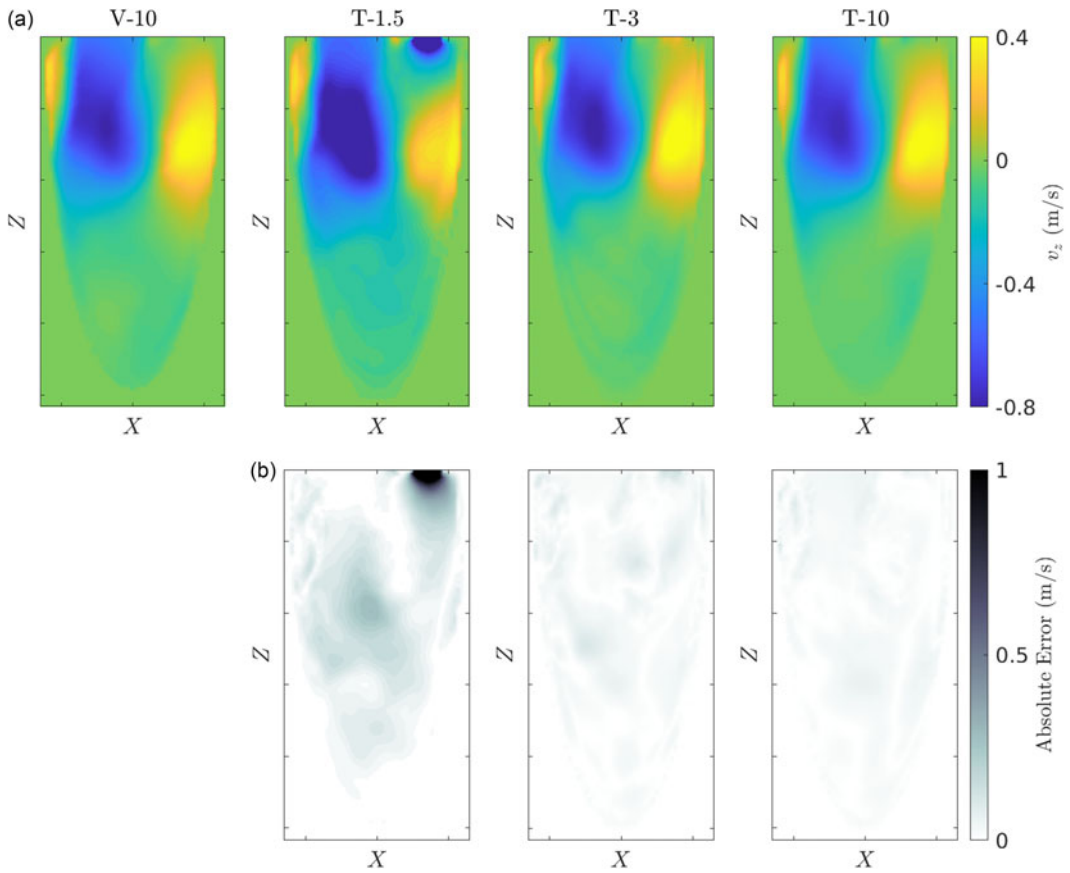


Figure 7. Comparison of the v_z velocity component in the $A-A'$ plane at $t^* = 19.25$ for the *Ideal 1* case using ROMs constructed from training sets T-1.5, T-3 and T-10 (a), along with the corresponding absolute error with respect to the reference case V-10 (b). The results displayed are using a selected subset of modes and a zero-growth rate ($\delta = 0$) enforced.

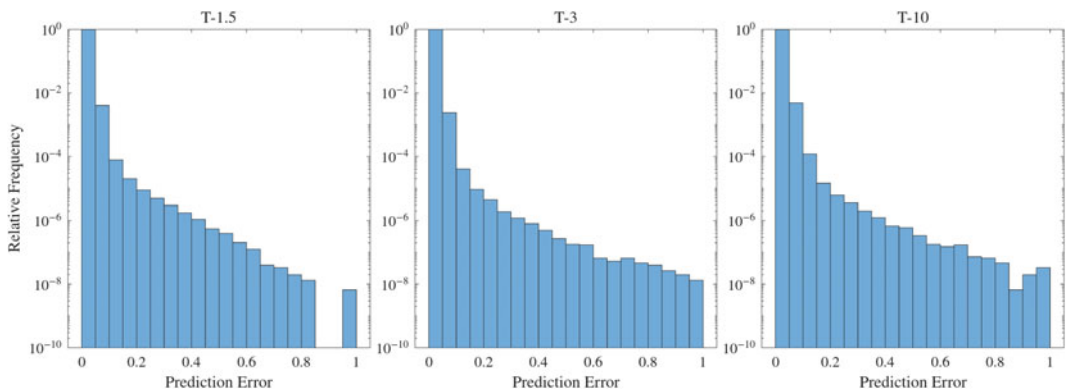


Figure 8. Histogram of the absolute error E using 20 bins for the *Ideal 1* model (each bin corresponds to 5% of error).

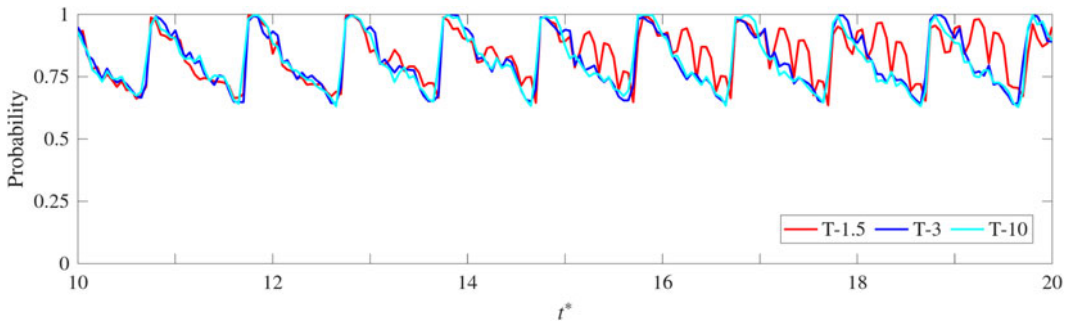


Figure 9. Temporal evolution of the probability that the predicted data remain within a 5% absolute error for the *Ideal 1* model across the 10 predicted cycles.

required approximately 38 hr to compute 10 cardiac cycles with a well-resolved mesh configuration. In contrast, the training phase, which involved exploring 10 different combinations of the truncation tolerance ε and window size d to ensure robust selection of physically relevant modes, took only 20 min and 14 s (for the case with 10 training cycles). The ROM prediction over the same time span was completed in just 36 s, yielding a SUF of 4.4×10^4 . Although the training cost adds a small overhead, it remains negligible compared with the full CFD runtime. Furthermore, the training cost scales approximately linearly with the number of snapshots and the number of calibration cases, and can be optimized through parallelization or by using a reduced dataset during calibration.

However, a trade-off must be established between computational savings and reconstruction accuracy. While shorter training windows significantly reduce the offline cost, as observed in case T-1.5, the ROM derived from such an economic (but poor) dataset may fail to capture essential flow features, leading to poor performance. In contrast, our analysis shows that using three cycles (case T-3) attains a reasonable balance: it provides sufficient temporal information to capture the dominant dynamics with acceptable accuracy, while still offering notable reductions in computational effort compared with longer simulations such as T-10.

4.2. Experimentally derived model: *Ideal 2*

Having analysed the tuning and performance of the ROM with the first idealized geometry, we now extend our study to the *Ideal 2* model. This serves as a test case to evaluate the method's performance on a different geometry, where the intraventricular flow dynamics are notably different and evolve at a slower pace. More details about the flow patterns and the development of flow instabilities in this geometry can be found in Lazpita *et al.* (2025).

The frequency accuracy obtained with HODMD is comparable to the *Ideal 1* case shown in figure 5; thus, a detailed analysis is omitted for brevity. It is important to recall, however, that although the dominant frequency was accurately captured using only 1.5 cycles, the associated growth rate was not. As a result, improving the temporal predictions required either increasing the number of cycles or enforcing a zero-growth rate. As before, the following results are obtained using a subset of selected modes with an enforced zero-growth rate ($\delta = 0$).

A central part of the analysis focuses on the evolution of the v_x velocity component along the centre line (L1) within the chamber. This evaluation compares ROM predictions with the original CFD data. Figure 10 presents the temporal evolution of v_x at L1 using a selected subset of modes enforcing zero-growth rate ($\delta = 0$). The absolute error between the ROM predictions and the reference data is also shown.

In this case, the flow exhibits slower dynamics due to smaller volume variations when compared with the *Ideal 1* configuration (Lazpita *et al.* 2025). This adds new challenges to the prediction task.

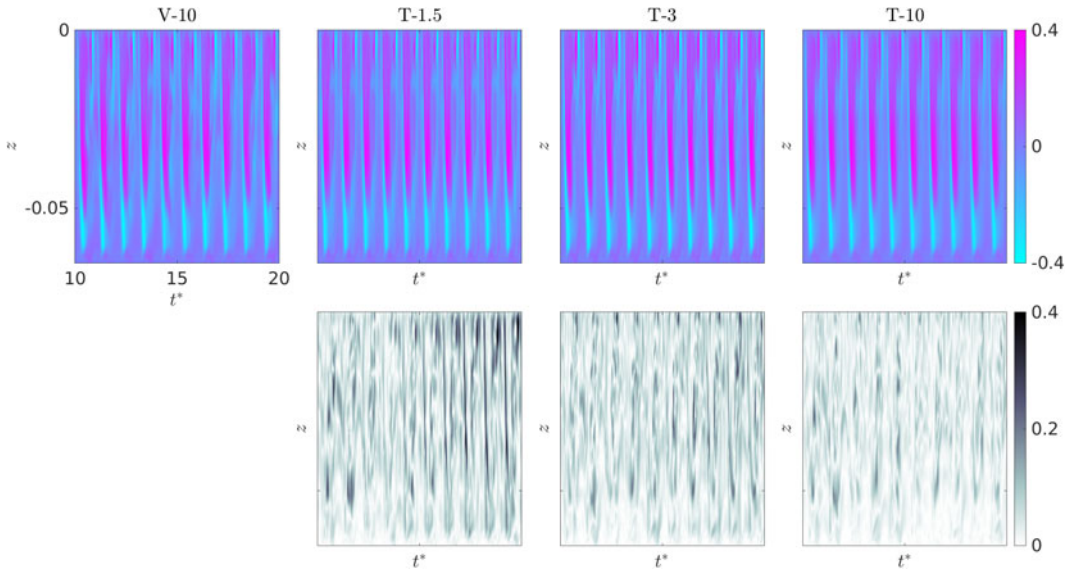


Figure 10. Counterpart of figure 6 for the *Ideal 2* model.

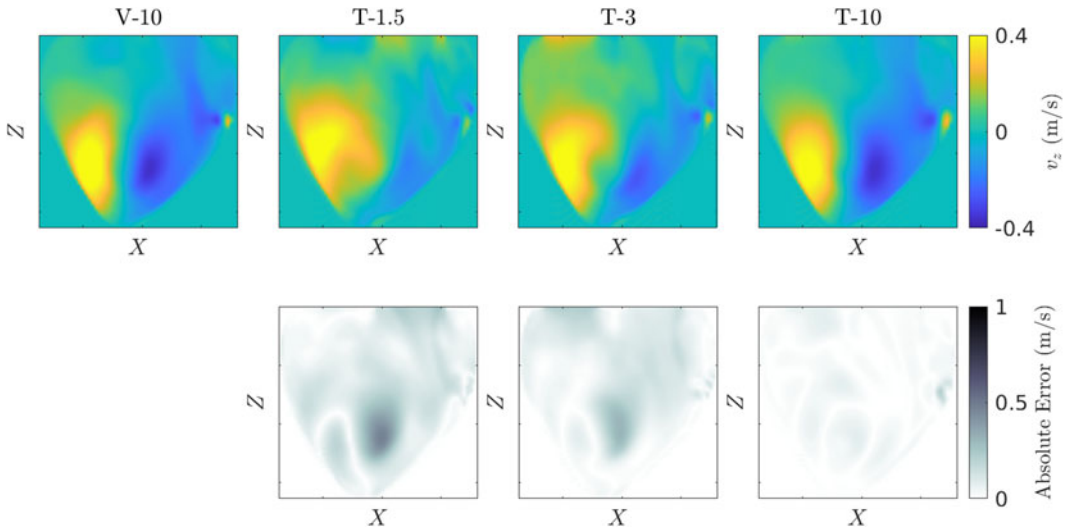


Figure 11. Counterpart of figure 7 for the *Ideal 2* model.

The model trained with only 1.5 cycles shows the highest error, although the error levels are comparatively smaller than for the 1.5 cycles case. Increasing the training set length to three cycles improves the predictions, yet the accuracy remains limited and comparable to that achieved with 10 cycles.

Again, spatial resolution is assessed in figure 11, showing the contours of the v_z velocity component in the A–A’ plane at $t^* = 19.25$ (1/4 of cycle) for the configurations yielding the most accurate results for the cases T-1.5, T-3 and T-10, along with the associated absolute error computed against the reference case V-10 for the *Ideal 2* case. The analysis of the two-dimensional contours in this geometry reveals that, for the T-1.5 case, the error is already quite low, although some localized inaccuracies remain. Nevertheless, the general flow features are well captured. Accuracy improves notably when the ROM is constructed using three cycles (T-3), and is significantly enhanced for the T-10 case, where the training data is richer. Despite this, the results obtained with T-3, or even T-1.5, are particularly appealing given

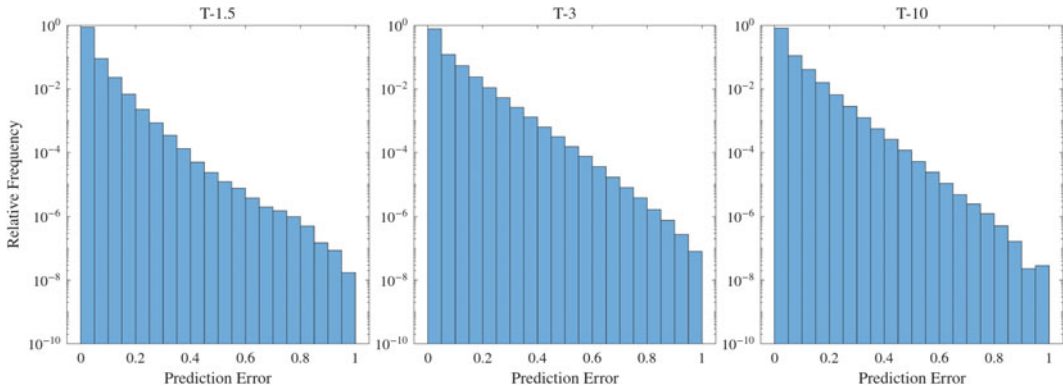


Figure 12. Counterpart of figure 8 for the Ideal 2 model.

the substantial computational savings achieved when only 1.5 or three cycles are needed instead of 10 or more (see later).

Comparing these results with the ones obtained in Ideal 1 § 4.1, the results for 1.5 cycles have improved, while T-3 or T-10 both offer good results for either model. This could be linked to the simpler vortex evolution that the second model has compared with the complex early breakdown seen in the first one (see Lazpita *et al.* 2025), which makes the dynamics easier to capture.

As before, we use error histograms to assess the relative frequency of different error magnitudes. Figure 12 shows the distribution of the normalized absolute error across predictions. The relative frequency of errors below 5% is close to 90%, indicating accurate overall performance, even though the overall error is slightly higher than in Ideal 1.

These results are even more pronounced in terms of computational cost reduction, as reflected in the SUF. In this idealized model, the high-fidelity CFD simulation required 48 hours on 40 CPUs to compute the cycles between $t = 10$ and $t = 20$. By contrast, the training phase, again exploring 10 combinations of ε and d for robust mode selection, took 22 min and 33 s. The ROM executed the same cycles in just 41 s, yielding an SUF of 5.1×10^4 . As in Ideal 1, the training cost represents only a minor fraction of the full-order simulation and can be further optimized with parallelization or reduced calibration datasets.

As already discussed at the end of § 4.1, there is a trade-off between ROM accuracy and computational cost. For this second model, training with 1.5 or three cycles greatly reduces data and offline cost compared with the full 10 cycles, while maintaining acceptable accuracy even for T-1.5. Nonetheless, T-3 should be preferred for improved performance.

5. Conclusions

This work introduced a predictive ROM based on HODMD to accelerate data acquisition in idealized intraventricular flow simulations, offering a faster alternative to full CFD. Unlike previous applications focused on data reconstruction (Corrochano *et al.* 2024; Lazpita *et al.* 2022; Lazpita *et al.* 2024), the proposed model predicts flow evolution by constructing a modal expansion and fitting the temporal dynamics of dominant modes. While similar ROMs have been used in other fluid contexts (Le Clainche & Vega 2017*a,b*), this is, to the authors' knowledge, the first time such an approach is applied to cardiac flows with moving walls and complex, time-varying geometries.

The ROM was tested on two contrasting cases: one with early vortex breakdown (Ideal 1) and another with a more stable VR (Ideal 2). The HODMD enabled robust mode extraction from short training sequences, effectively filtering noise and transient features. Enforcing zero-growth rates further stabilized long-term predictions.

Results showed that the ROM accurately reproduced key flow patterns and frequencies, including vortex formation and breakdown. When combined with spectral filtering, the model improved interpretability and reduced sensitivity to spurious components.

Quantitatively, the ROM yielded low relative errors and high spatial–temporal correlation with CFD results, even with minimal training data. Predictions ran in seconds on a laptop versus hours for full CFD, achieving SUFs of $O(10^5)$. Training with three cycles offered a good balance between efficiency and accuracy. However, the study also highlights that very short training windows (e.g. 1.5–3 cycles), commonly used in prior work, may fail to capture the full dynamics, emphasizing the need for longer time series.

In terms of computational efficiency, it is worth distinguishing between projection-based and data-driven ROM approaches. Among the former, the most employed techniques in the literature include Galerkin-projection ROMs (Kalashnikova & Barone 2010; Rapún & Vega 2018), which project the governing equations onto a reduced modal subspace. Although these methods are physics-based and capable of capturing the dominant flow structures, they often require the definition of appropriate closure models to maintain stability, and their implementation can become cumbersome for complex three-dimensional or unsteady configurations.

Data-driven approaches, by contrast, do not rely on the explicit projection of the governing equations. Within this category, we find both the HODMD method proposed here and other machine-learning-based models, such as autoencoders or convolutional and recurrent neural networks. While purely deep learning models can yield fast predictions once trained (Sanchis-Agudo *et al.* 2024; Solera-Rico *et al.* 2024), they generally require large training datasets, extensive hyperparameter optimization, and problem-specific architectures, which may limit their generalization and interpretability.

The proposed HODMD framework, on the other hand, directly extracts coherent structures and their characteristic frequencies from data, providing a compact and physically interpretable representation of the flow. It requires minimal tuning, remains fully data-driven, and achieves a favourable trade-off between accuracy, interpretability, and computational cost. Moreover, its direct applicability to both CFD and experimental (e.g. medical imaging) data makes it a robust and versatile tool for future cardiovascular flow studies.

The present analysis focuses on the large-scale dynamics of the VR generated during early diastole, which has been shown in previous works (He *et al.* 2022; Vedula *et al.* 2014; Zheng *et al.* 2012; Tagliabue *et al.* 2017) to be accurately captured under laminar flow assumptions. This simplification is therefore sufficient for studying the main mechanisms of efficient intraventricular filling. In addition, the ROM developed here inherently filters out small-scale noise, providing a clear representation of the dominant coherent structures.

Nevertheless, if the objective were to reconstruct or predict transitional or turbulent regimes, the methodology could be extended to incorporate uncertainty quantification or stochastic modelling techniques, allowing the ROM to account for smaller-scale flow fluctuations. In fact, the HODMD framework has already demonstrated strong performance in turbulent and transitional configurations in other fields, including wind turbine aerodynamics (Ferrer & Le Clainche 2019; Le Clainche & Ferrer 2018) and complex fluid flows (Beltrán *et al.* 2022; Le Clainche & Vega 2017b; Kou *et al.* 2018), confirming its versatility and robustness across a wide range of flow regimes.

It is worth noting that the ROM developed in this study is fully data-driven and physics-based, which makes its extension to patient-specific cases straightforward. Once the input database is available, either from CFD simulations or medical imaging, the same methodology can be directly applied to anatomies with more irregular geometries or pathological conditions. The model does not rely on any geometrical simplification, and its ability to learn dominant spatiotemporal flow features from data ensures its adaptability to complex cardiac configurations.

In summary, this HODMD-based ROM delivers accurate, interpretable, and highly efficient predictions of intraventricular flow, with potential for real-time applications and fast parametric studies. Future work will extend this framework to patient-specific anatomies, clinical data integration and pathological scenarios.

Supplementary data. Supplementary information, codes and databases are available at <https://modelflows.github.io/modelflowsapp/>.

Acknowledgements. The authors gratefully acknowledge Professor Vedula for kindly providing the geometry data of *Ideal 2* model that was essential for conducting this study.

Data availability statement. The data that support the findings of this study are available upon reasonable request. Should the reader wish to gain a more detailed understanding of the process by which the databases were obtained, as well as other pertinent information, they are invited to visit the following website, where they will find the relevant codes and tutorials in DigitHEART (0000).

Author contributions. E.L. performed the simulations, processed and visualized the results, and drafted the manuscript. E.L., J.G.M. and S.L.C. jointly conceived the analysis and contributed to the interpretation and discussion of the findings. J.G.M. and S.L.C. supervised the study, assisted in manuscript preparation and provided critical feedback throughout the project. All authors have read and approved the final version of the manuscript.

Funding statement. The authors acknowledge the grant PLEC2022-009235 funded by MCIN/AEI/ 10.13039/501100011033 and by the European Union ‘NextGenerationEU’/PRTR and the grant PID2023-147790OB-I00 funded by MCIU/AEI/10.13039/501100011033/FEDER, UE. The authors gratefully acknowledge the Universidad Politécnica de Madrid (www.upm.es) for providing computing resources on Magerit Supercomputer.

Competing interests. The authors declare no conflict of interest.

Ethical standards. The research meets all ethical guidelines, including adherence to the legal requirements of the study country.

References

- Africa, P. C., Fumagalli, I., Bucelli, M., Zingaro, A., Fedele, M., Dede', L., & Quarteroni, A. (2024). Quarteroni, etal, lifex-cfd: An open-source computational fluid dynamics solver for cardiovascular applications. *Computer Physics Communications*, 296, 109039. <https://doi.org/10.1016/j.cpc.2023.109039>
- Ansys, inc (2023). *Ansys fluent academic research, Release 2023 R1, help system*. Ansys Fluent Theory Guide.
- Ballarin, F., Faggiano, E., Ippolito, S., Manzoni, A., Quarteroni, A., Rozza, G., & Scrofani, R. (2016). Fast simulations of patient-specific haemodynamics of coronary artery bypass grafts based on a Pod–Galerkin method and a vascular shape parametrization. *Journal of Computational Physics*, 315, 609–628. <https://doi.org/10.1016/j.jcp.2016.03.065>
- Beltrán, V., Clainche, S. Le, & Vega, J. M. (2022). An adaptive data-driven reduced order model based on higher order dynamic mode decomposition. *Journal of Scientific Computing*, 92(12). <https://doi.org/10.1007/s10915-022-01855-2>.
- Canè, F., Delcour, L., Luigi Redaelli, A. C., Segers, P., & Degroote, J. (2022). A CFD study on the interplay of torsion and vortex guidance by the mitral valve on the left ventricular wash-out making use of overset meshes (Chimera technique). *Frontiers in Medical Technology*, 4, 1018058. <https://doi.org/10.3389/fmedt.2022.1018058>
- Chnafa, C., Mendez, S., & Nicoud, F. (2014). Image-based large-eddy simulation in a realistic left heart. *Computers & Fluids*, 94, 173–187. <https://doi.org/10.1016/j.compfluid.2014.01.030>
- Le Clainche, S., & Ferrer, E. (2018). A reduced order model for temporal forecasting of flows around vertical axis wind turbines. *Energies*, 11(3), 566. <https://doi.org/10.3390/en11030566>
- Le Clainche, S., Izbassarov, D., Rosti, M., Brandt, L., & Tammisola, O. (2020). Coherent structures in the turbulent channel flow of an elastoviscoplastic fluid. *Journal of Fluid Mechanics*, 888, A5. <https://doi.org/10.1017/jfm.2020.31>
- Le Clainche, S., & Vega, J. M. (2017a). Higher order dynamic mode decomposition. *SIAM Journal on Applied Dynamical Systems*, 16(2), 882–925. <https://doi.org/10.1137/15M1054924>
- Le Clainche, S., & Vega, J. M. (2017b). Higher order dynamic mode decomposition to identify and extrapolate flow patterns. *Physics of Fluids*, 29(8). <https://doi.org/10.1063/1.4997206>
- Corrochano, A., D’Alessio, G., Parente, A., & Le Clainche, S. (2024). Hierarchical higher-order dynamic mode decomposition for clustering and feature selection. *Computers & Mathematics with Applications*, 158, 36–45. <https://doi.org/10.1016/j.camwa.2024.01.003>
- Domenichini, F., & Pedrizzetti, G. (2016). Hemodynamic forces in a model left ventricle. *Physical Review Fluids*, 1(8), 083201. <https://doi.org/10.1103/PhysRevFluids.1.083201>
- Domenichini, F., Pedrizzetti, G., & Baccani, B. (2005). Three-dimensional filling flow into a model left ventricle. *Journal of Fluid Mechanics*, 539, 179–198. <https://doi.org/10.1017/S0022112005005550>
- Domenichini, F., Querzoli, G., Cenedese, A., & Pedrizzetti, G. (2007). Combined experimental and numerical analysis of the flow structure into the left ventricle. *Journal of Biomechanics*, 40(9), 1988–1994. <https://doi.org/10.1016/j.jbiomech.2006.09.024>

- Ferrer, E., & Clainche, S. Le (2019). Simple models for cross flow turbines. In *Recent advances in CFD for Wind and Tidal Offshore Turbines* (pp. 83–93). Springer. https://doi.org/10.1007/978-3-030-11887-7_1
- Groun, N., Villalba-Orero, M., Casado-Martín, L., Lara-Pezzi, E., Valero, E., Le Clainche, S., & Garicano-Mena, J. (2025). Eigenhearts: Cardiac diseases classification using eigenfaces approach. *Computers in Biology and Medicine*, 192, 110167. <https://doi.org/10.1016/j.combiomed.2025.110167>
- Grünwald, A., Korte, J., Wilmanns, N., Winkler, C., Linden, K., Herberg, U., Groß-Hardt, S., Steinseifer, U., & Neidlin, M. (2022). Intraventricular flow simulations in singular right ventricles reveal deteriorated washout and low vortex formation. *Cardiovascular Engineering and Technology*, 1–9. <https://doi.org/10.1007/s13239-021-00598-9>
- He, G., Han, L., Zhang, J., Shah, A., Kaczorowski, D. J., Griffith, B. P., & Wu, Z. (2022). Numerical study of the effect of LVAD inflow cannula positioning on thrombosis risk. *Computer Methods in Biomechanics and Biomedical Engineering*, 25(8), 852–860. <https://doi.org/10.1080/10255842.2021.1984433>
- Hetherington, A., Corrochano, Aán, Abadía-Heredia, R., Lazpita, E., Muñoz, E., Díaz, P., Maiora, E., López-Martín, M., & Le Clainche, S. (2024). Modelflows-app: Data-driven post-processing and reduced order modelling tools. *Computer Physics Communications*, 301, 109217. <https://doi.org/10.1016/j.cpc.2024.109217>
- Kalashnikova, I., & Barone, M. F. (2010). On the stability and convergence of a Galerkin reduced order model (ROM) of compressible flow with solid wall and far-field boundary treatment. *International Journal for Numerical Methods in Engineering*, 83(10), 1345–1375. <https://doi.org/10.1002/nme.2867>
- Kheradvar, A., Pedrizzetti, G., Kheradvar, A., & Pedrizzetti, G. (2012). *Vortex formation in the heart*. Springer. https://doi.org/10.1007/978-1-4471-2288-3_3
- Kilner, P. J., Yang, G.-Z., Wilkes, A. J., Mohiaddin, R. H., Firmin, D. N., & Yacoub, M. H. (2000). Asymmetric redirection of flow through the heart. *Nature*, 404, 759–761. <https://doi.org/10.1038/35008075>
- Kjeldsberg, H. A., Sundnes, J., & Valen-Sendstad, K. (2023). A verified and validated moving domain computational fluid dynamics solver with applications to cardiovascular flows. *International Journal for Numerical Methods in Biomedical Engineering*, 39(6), e3703. <https://doi.org/10.1002/cnm.3703>
- Korte, J., Rauwolf, T., Thiel, J.-N., Mitrasch, A., Groschopp, P., Neidlin, M., Schmeißer, A., Braun-Dullaues, R., & Berg, P. (2023). Hemodynamic assessment of the pathological left ventricle function under rest and exercise conditions. *Fluids*, 8(2), 71. <https://doi.org/10.3390/fluids8020071>
- Kou, J., Clainche, S. Le, & Zhang, W. (2018). A reduced-order model for compressible flows with buffeting condition using higher order dynamic mode decomposition with a mode selection criterion. *Physics of Fluids*, 30, 016103. <https://doi.org/10.1063/1.4999699>
- Lassila, T., Manzoni, A., Quarteroni, A., & Rozza, G. (2014). Model order reduction in fluid dynamics: Challenges and perspectives. *Reduced Order Methods for Modeling and Computational Reduction*, 235–273. https://doi.org/10.1007/978-3-319-02090-7_9
- Lazpita, E., Garicano-Mena, J., Paniagua, G., Le Clainche, S., & Valero, E. (2024). A data-driven sensibility tool for flow control based on resolvent analysis. *Results in Engineering*, 22, 102070. <https://doi.org/10.1016/j.rineng.2024.102070>
- Lazpita, E., Mares, A., Quintero, P., Garicano-Mena, J., & Le Clainche, S. (2024). Modeling heart flow dynamics using numerical simulations to identify the vortex ring: A practical guide. *Results in Engineering*, 24, 103644. <https://doi.org/10.1016/j.rineng.2024.103644>
- Lazpita, E., Martínez-Sánchez, Á., Corrochano, A., Hoyas, S., Clainche, S. Le, & Vinuesa, R. (2022). On the generation and destruction mechanisms of arch vortices in urban fluid flows. *Physics of Fluids*, 34(5). <https://doi.org/10.1063/5.0088305>
- Lazpita, E., Nagargoje, M., Clainche, S., & Garicano-Mena, J. (2024). On the numerical simulation of left ventricle models. In *ECCOMAS 2024*. https://www.scipedia.com/public/Lazpita_et_al_2024a
- Lazpita, E., Neidlin, M., Garicano-Mena, J., & Clainche, S. L. (2025). Characterizing intraventricular flow patterns via modal decomposition techniques in idealized left ventricle models. [arXiv:2507.21651](https://arxiv.org/abs/2507.21651).
- Meschini, V., De Tullio, M. D., Querzoli, G., & Verzicco, R. (2018). Flow structure in healthy and pathological left ventricles with natural and prosthetic mitral valves. *Journal of Fluid Mechanics*, 834, 271–307. <https://doi.org/10.1017/jfm.2017.725>
- Meschini, V., Mittal, R., & Verzicco, R. (2021). Systolic anterior motion in hypertrophic cardiomyopathy: a fluid–structure interaction computational model. *Theoretical and Computational Fluid Dynamics*, 35(3), 381–396. <https://doi.org/10.1007/s00162-021-00564-0>
- Mezić, I. (2013). Analysis of fluid flows via spectral properties of the Koopman operator. *Annual Review of Fluid Mechanics*, 45(1), 357–378. <https://doi.org/10.1146/annurev-fluid-011212-140652>
- DigitHEART: new tools and models for predicting heart disease progression and treatment response. ModelFLOws-cardiac. Available at accessed: 2025–04–23. <https://modelflows.github.io/modelflowsapp/cardiacpathologydetection/>
- Nagargoje, M. S., Lazpita, E., Garicano-Mena, J., & Clainche, S. Le (2025). A review on vortex dynamics in the healthy and dilated left ventricles and its application to heart health. *Flow*, 5, E10. <https://doi.org/10.1017/fo.2025.6>
- Otto, S. E., & Rowley, C. W. (2021). Koopman operators for estimation and control of dynamical systems. *Annual Review of Control, Robotics, and Autonomous Systems*, 4(1), 59–87. <https://doi.org/10.1146/annurev-control-071020-010108>
- Pedrizzetti, G., & Domenichini, F. (2015). Left ventricular fluid mechanics: The long way from theoretical models to clinical applications. *Annals of Biomedical Engineering*, 43, 26–40. <https://doi.org/10.1007/s10439-014-1101-x>
- Quarteroni, A., Lassila, T., Rossi, S., & Ruiz-Baier, R. (2017). Integrated heart—coupling multiscale and multiphysics models for the simulation of the cardiac function. *Computer Methods in Applied Mechanics and Engineering*, 314, 345–407. <https://doi.org/10.1016/j.cma.2016.05.031>

- Rapún, M. L., & Vega, J. M. (2018). Reduced order models based on local POD plus gGalerkin projection. *Journal of Computational Physics*, 229(8), 3046–3063. <https://doi.org/10.1016/j.jcp.2009.12.029>
- Sanchis-Agudo, M., Wang, Y., Arnau, R., Guastoni, L., Lim, J., Duraisamy, K., & Vinuesa, R. (2024). Easy attention: A simple attention mechanism for temporal predictions with transformers. *APL Computational Physics*, 1(1).
- Schmid, P. J. (2010). Dynamic mode decomposition of numerical and experimental data. *Journal of Fluid Mechanics*, 656, 5–28. <https://doi.org/10.1017/S0022112010001217>
- Sengupta, P. P., Korinek, J., Belohlavek, M., Narula, J., Vannan, M. A., Jahangir, A., & Khandheria, B. K. (2006). Left ventricular structure and function: Basic science for cardiac imaging. *Journal of the American College of Cardiology*, 48(10), 1988–2001. <https://doi.org/10.1016/j.jacc.2006.08.030>
- Sirovich, L. (1987). Turbulence and the dynamics of coherent structures. I. Coherent structures. *Quarterly of Applied Mathematics*, 45(3), 561–571. <https://www.ams.org/journals/qam/1987-45-03/S0033-569X-1987-0910462-6/>
- Solera-Rico, A., Vila, C. Sanmiguel, Gómez-López, M., Wang, Y., Almashjary, A., Dawson, S. T. M., & Vinuesa, R. (2024). β -variational autoencoders and transformers for reduced-order modelling of fluid flows. *Nature Communications*, 15(1), 1361.
- Spandan, V., Meschini, V., Ostilla-Mónico, R., Lohse, D., Querzoli, G., De Tullio, M. D., & Verzicco, R. (2017). A parallel interaction potential approach coupled with the immersed boundary method for fully resolved simulations of deformable interfaces and membranes. *Journal of Computational Physics*, 348, 567–590. <https://doi.org/10.1016/j.jcp.2017.07.036>
- Tagliabue, A., Dedè, L., & Quarteroni, A. (2017). Complex blood flow patterns in an idealized left ventricle: A numerical study. *Chaos: An Interdisciplinary Journal of Nonlinear Science*, 27(9). <https://doi.org/10.1063/1.5002120>
- Thomas, J. D., & Popovic, Z. B. (2006). Assessment of left ventricular function by cardiac ultrasound. *Journal of the American College of Cardiology*, 48(10), 2012–2025. <https://doi.org/10.1016/j.jacc.2006.06.071>
- Vedula, V., Fortini, S., Seo, J. H., Querzoli, G., & Mittal, R. (2014). Computational modeling and validation of intraventricular flow in a simple model of the left ventricle. *Theoretical and Computational Fluid Dynamics*, 28, 589–604. <https://doi.org/10.1007/s00162-014-0335-4>
- World Health Organization. (2024). *Cardiovascular diseases (cvds) - fact sheet*. [https://www.who.int/news-room/fact-sheets/detail/cardiovascular-diseases-\(cvds\)](https://www.who.int/news-room/fact-sheets/detail/cardiovascular-diseases-(cvds))
- Zheng, X., Seo, J. H., Vedula, V., Abraham, T., & Mittal, R. (2012). Computational modeling and analysis of intracardiac flows in simple models of the left ventricle. *European Journal of Mechanics - B/Fluids*, 35, 31–39. <https://doi.org/10.1016/j.euromechflu.2012.03.002>